ACS OMEGA

Open Access

http://pubs.acs.org/journal/acsodf

Article

Synthesis, Characterization, and Application of Amorphous Silica−Aluminas Support for Fischer−Tropsch Wax Hydrocracking Catalysts

Tao Li, Shuyuan Wang, Zhenye Sun, Yan Wang, Jinghong Su, Yinghui Lv, Ling Zhang, Zhichao Tao,* and Yong Yang*

Cite This: *ACS Omega* 2024, 9, 36741−36750

Read Online

ACCESS | Metrics & More | Article Recommendations | Supporting Information

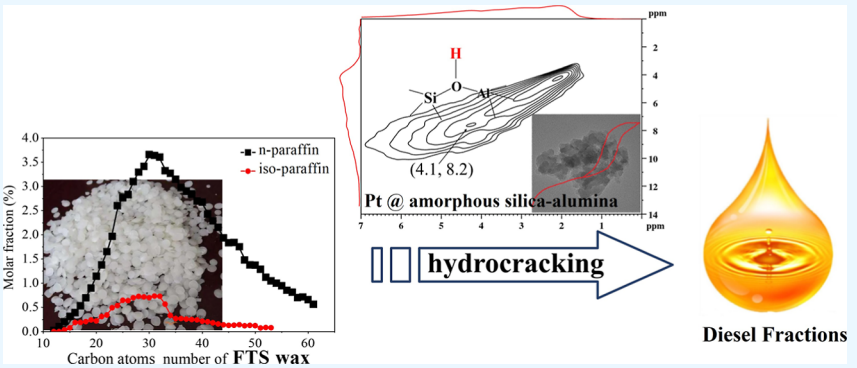

ABSTRACT: High-performance amorphous silica−aluminas (ASAs) were prepared prior to the formation of the 10-membered ring (10-MR) ZSM-5 zeolite by regulating the hydrothermal processing time. Their structures, morphologies, acidity properties, and Si−Al coordination were well studied. Particularly, a facile FTIR method of in-situ adsorbing bulky 2,6-dimethlypyridine followed by pyridine adsorption was innovatively utilized to quantify the Brønsted acid sites in micropores. All the ASAs samples were transformed into catalysts by loading with 0.5 wt % Pt. The structure−activity relationship, especially from the strength, density, and location of Brønsted acid sites, was investigated by Fischer−Tropsch synthesis (FTS) wax hydrocracking. The evaluation results showed that the medium strong Brønsted acid sites located on the external surface played a crucial role in the activity. Contrary to the general belief that larger pores favor the production of heavy cracking fractions, the ASAs with a 10-MR microporous structure proved to be more effective for diesel production than those with a 12-membered ring (12-MR). Strong Brønsted acid sites in micropores were less conducive to diesel production mainly due to stronger adsorption at these sites and steric hindrance from the microporous system. Furthermore, the Pt/AS-20 catalyst with few intramicropore Brønsted acid sites exhibited high diesel selectivity (83.3%) at 50.5% conversion under industrially relevant reaction conditions, which provides a significant opportunity to develop FTS wax hydrocracking catalysts more rationally.

1. INTRODUCTION

Fischer−Tropsch synthesis (FTS) is a technology of great potential to produce clean *n*-alkanes (>90%) from syngas, while the latter can vary from various fossil sources (natural gas or coal) to renewable biomass.[1] As the main product of the large-scale industrial application of FTS (accounting for over 50%), FTS wax is highly paraffinic (C_{20}−C_{80}) and virtually free of nitrogen, sulfur, and aromatics, making it ideal to produce environmental friendly clean diesel fractions through hydrocracking.[2,3] This reaction is achieved using a bifunctional catalyst characterized by the presence of metal sites with (de)hydrogenation function and acidic sites with isomerization-cracking function.[4−6] Solid acid supports, for example, amorphous oxides or/and zeolites, loaded with noble metal (e.g., Pt) have emerged as some of the most promising hydrocracking catalysts.[7,8] For converting the easily cracking and bulky FTS wax, amorphous silica−aluminas (ASAs) as catalyst supports become more prominent in providing moderate acid sites and facilitating molecular diffusion.[9,10]

ASAs-based hydrocracking catalysts have achieved significant attention for both scientific and practical application. Pölczmann et al.[11] evaluated Pt/Al-SBA-15 as a catalyst for the

Received: June 14, 2024
Revised: July 30, 2024
Accepted: July 31, 2024
Published: August 14, 2024

paraffin (C_{15}−C_{57}) conversion, and reported that mesoporous supports Al-SBA-15 supports were more effective than SAPO-11 zeolite-type materials in producing gas oil (C_{11}−C_{20}) and base oil (C_{21}−C_{29}). Moreover, the spacious pore system in Pt/Al-SBA-15 catalyst favored the production of branched paraffins, achieving up to 70% selectivity for iso-paraffin at 623 K. Liu et al.[12] investigated the FTS wax hydrocracking over Pt-modified polyoxocation-pillared montmorillonites, revealing that the moderate or "appropriately weak" acid sites, which promote olefin desorption, are ideal to produce diesel-grade hydrocarbons. Lee et al.[8] elucidated the influence of the density (concentration) and types of acid sites in ASAs on the paraffin (C_{21}−C_{34}) hydrocracking, revealing that the catalytic performance was mainly dependent on the Brønsted acid sites instead of Lewis acid sites. Another similar study noted that the wax (C_{21}−C_{34}) conversion increased with the total acid sites density, while the yield of middle fractions (C_{10}−C_{20}) exhibited a volcano-shaped curve. Furthermore, Pd/SA-40 with moderate acidity showed the highest middle distillate yield (45.1%) at 76.0% conversion.[13] Although numerous studies have explored the preparation and application of ASAs-type catalysts, few have investigated the prospects of ASAs from the perspective of acid site location and type using industrialized FTS wax (C_{20}−C_{80}) as feedstock.[14−16] In previous work, we reported a facile method for synthesizing high diesel selective ASAs support from a precursor before the formation of 12-member ring (12-MR) BEA topological zeolite.[17] The catalytic evaluation results showed that the primary cracking products (<C_{40}) from initial FTS wax hydrocracking can penetrate into the three-dimensional 12-MR micropores, which increases the potential for multicracking to produce naphtha or liquefied petroleum gas (LPG), causing a decrease in diesel selectivity.[17] Therefore, minimizing the diffusion of these products to micropores and reducing multicracking occurrence is crucial for maximizing diesel selectivity. Inspired by this, the ASAs obtained from the mother liquid of 10-MR MFI zeolite before the long-range crystal order formation not only meet the aforementioned requirements but also enrich the understanding of FTS wax hydrocracking catalyst development.

Appropriate characterization of the acidity details is a prerequisite for this work. Fourier transform infrared spectroscopy (FTIR) of adsorbing substituted alkylpyridine is commonly used method to provide information on acidic sites systems.[18,19] To obtain the desired information, the acidic sites at different position must be accessible to the basic probe molecules used, guiding the selection of alkylpyridines with appropriate dynamic sizes.[18,19] Some authors have characterized the acidity of 10-MR zeolite applying pyridine (Py)-FTIR and 2,6-dimethlypyridine (DMPy)-FTIR, to collect the densities of total Brønsted acid sites and those on the external surface, respectively.[20−22] However, the quantified acidic information calculated from the Lambert−Beer Law varies with the integrated molar extinction coefficients (IMEC) of alkylpyridines.[23,24] Additionally, due to the difference in the units of quantification between Py-FTIR (μmol Py/g) and DMPy-FTIR (μmol DMPy/g) spectra, the variation of the Brønsted acidity in micropores was not available. This limits the understanding of the acidic nature and structure−activity relationships for the solid-acid catalyst containing 10-MR pore topology.

In this work, a series of ASAs were synthesized from a 10-MR ZSM-5 zeolite precursor solution after a variable hydrothermal synthesis time. Their physicochemical properties were studied using an array of multicharacterization techniques. Particularly, a facile FTIR method of in-situ preferentially adsorbing DMPy probe molecules followed by Py adsorption was innovatively utilized to quantify the Brønsted acid sites in micropores. After all of the protonic ASAs were impregnated with a required Pt-containing solution, the structure−activity relationship between ASAs supports and catalytic performance was studied using FTS wax hydrocracking to diesel as a model reaction, highlighting a direction for designing efficient hydrocracking catalysts for the FTS wax feedstock.

2. EXPERIMENTAL SECTION

2.1. Chemicals and Reagents. All reagents were used without further purification, and their detailed descriptions are available in the Supporting Information.

2.2. Catalysts Preparation. The ASAs samples were prepared by a static hydrothermal method, and the theoretical molar ratio of the initial gel was 1.0 Al_2O_3/50 SiO_2/5.1 NaOH/10.7 TPAOH/2000H_2O. Sodium hydroxide and TPAOH were orderly added into distilled water with stirring. After sufficient dissolution, sodium aluminate was added into the solution and then silica sol, under vigorous stirring at 25 °C overnight. Subsequently, the resulting well-mixed gel was transferred to 800 mL autoclaves for static crystallization at 115 °C with hydrothermal synthesis times varying between 20 and 96 h. The resulting solid samples were filtered, washed with distilled water, dried overnight at 100 °C and then calcined for 5 h at 550 °C. Finally, the proton ASAs samples were ion-exchanged by 0.5 M NH_4Cl solution, then dried and calcined in a muffle furnace at 550 °C for 3 h. The as-prepared ASAs samples were labeled as AS-x (AS-20, AS-40, AS-47, AS-55, AS-62, AS-96), where x denotes hydrothermal synthesis times of 20, 40, 47, 55, 62 and 96 h, respectively.

The obtained ASAs samples were shaped into 20−40 mesh. And the nominal platinum content was 0.5 wt % by wet impregnation of $Pt(NH_3)_4Cl_2{\cdot}XH_2O$ solution. After impregnation, the ASAs samples were dried for 6 h at 100 °C, and calcined for 3 h at 420 °C. The resulting catalysts supported on AS-20, AS-40, AS-47, AS-55, and AS-62 were labeled as Pt/AS-20, Pt/AS-40, Pt/AS-47, Pt/AS-55, and Pt/AS-62 respectively.

2.3. Samples Characterization. X-ray diffraction (XRD) patterns of the powdered material were obtained by using Cu Kα radiation (λ = 0.154059 nm) on a Bruker D8 ADVANCE diffractometer with an X-ray source operating at 40 kV and a current of 40 mA.

Scanning electron microscopy (SEM) measurements were carried out on an FEI QUANTA 400 microscope. Transmission electron microscopy (TEM) measurements were performed on an FEI Talos F200A electron microscope with a finite line resolution of 1.4 Å and an accelerating voltage of 200 kV.

The textural properties of the ASAs supports were measured by using a Micromeritics ASAP 2420 analyzer. First, samples were degassed at 350 °C for 6 h and then analyzed at liquid nitrogen temperature (−196 °C). The total surface area (S_{BET}) was calculated using the adsorption data by the Brunauer−Emmett−Teller (BET) equation. The total pore volume (V_{Pore}) was calculated via the single-point method based on the adsorption at P/P_o = 0.9736, whereas the micropore surface area (S_{Mic}) and mesoporous surface area (S_{Ext}) were derived by the *t*-plot method.

https://doi.org/10.1021/acsomega.4c05594
ACS Omega 2024, 9, 36741−36750

Ammonia temperature-programmed (NH_3-TPD) desorption measurements were carried out on a Micromeritics ASAP 2920 analyzer. Prior to analysis, the sample was heated in helium flow for 1 h at 600 °C to remove any possible impurities and then cooled down to 100 °C. Afterward, the sample was treated in a stream of NH_3 for 20 min before switched to helium for 30 min to remove physically adsorbed NH_3. The desorption process was conducted ranging from 100 to 600 °C with a ramp rate of 10 °C/min, and the desorbed NH_3 was recorded and analyzed using a mass spectrometer.

Fourier transform infrared (FTIR) spectra were obtained with a Bruker Vertex 70 spectrophotometer, to quantitatively study the Brønsted and Lewis acid sites distribution. In terms of Py-FTIR, the test sample was first pressed into a self-supporting wafer, followed by pretreating under vacuum for 1.0 h at 350 °C, and then cooled down to 30 °C. Afterward, the sample was saturated with Py vapor molecules, followed by evacuated for 30 min. The sample was desorbed at 200 and 350 °C, respectively, and the corresponding spectra were recorded. The peaks at 1548 and 1450 cm^{-1} were fitted as the Brønsted and Lewis acid, respectively.[25,26] And quantitative acidity information was calculated based on Lambert−Beer law and eqs 1 and 2.[23,26] A facile FTIR method of in situ adsorbing DMPy followed by adsorption of Py (DMPy-Py-FTIR) was utilized to quantify the acid sites in micropores and weaken the effect brought by IMEC. The pretreated self-supporting wafer samples were first saturated with DMPy vapor molecules instead of Py, and then evacuated for 1.0 h. The tested sample was then saturated with Py vapor, and the physically adsorbed one was removed by evacuation. Subsequently, the Py adsorption on the sample was measured by FTIR spectroscopy following the Py-FTIR evaluation procedure described above. The detailed procedures are referred to in refs 17 and 23.

$$C\ (\text{alkylpyridine on Brønsted}) = \frac{\pi \times R^2 \times IA(\text{B})}{\text{IMEC}(\text{alkylpyridine, on Brønsted}) \times \text{W}} \quad (1)$$

$$C\ (\text{alkylpyridine on Lewis}) = \frac{\pi \times R^2 \times \text{IA(L)}}{\text{IMEC}(\text{alkylpyridine, on Lewis}) \times W} \quad (2)$$

where C is the molar concentration (μmol alkylpyridine/g); IA is the integrated absorbance of Brønsted or Lewis band (cm^{-1}); W is the weight of sample disk (g); R is the radius of sample disk (cm); IMEC (Py on Brønsted) = 1.67 cm/μmol, IMEC (Py on Lewis) = 2.22 cm/μmol, as referred to in refs 23 and 24.

^{27}Al and ^{29}Si magic angle spinning (MAS) nuclear magnetic resonance (NMR) measurements were carried out on a Bruker AVANCE III 600 WB spectrometer to analyze the coordination states of aluminum and silicon species in ASAs samples. ^{1}H DQ MAS NMR spectra were collected via a POST-7 pulse sequence with indirect dimensional incremental intervals of 83 μs.

2.4. Catalyst Test. Catalytic performance was evaluated in a fixed-bed reactor at 4.0 MPa. The properties of the raw material for the reaction, FTS wax, are shown in ref 17. For each evaluation reaction, 2.8 g of 20−40 mesh catalyst was loaded into a stainless−steel reaction tube. Before formal sampling, the loaded catalyst was activated in situ with H_2 at 380 °C for 4 h at a flow rate of 100 mL/min, and then cooled to 200 °C. The melting raw material FTS wax was continuously pumped into the reactor at a set flow rate. In each catalyst test, 6 to 8 points were sampled. During the sampling period, the temperature was held constant for 24 h. The reaction off-gas was analyzed by an online gas chromatograph (Agilent 7890N) equipped with a flame ionization detector (FID), while the liquid products were analyzed by an off-line gas chromatograph (Agilent 7890B). The FTS wax conversion and products (C_{10}−C_{22}, as an example) selectivity were calculated based to the following two formulas 3 and 4

$$\text{wax conversion (\%)} = \frac{\text{wt \% of } C_{23+} \text{ in feed} - \text{wt \% of } C_{23+} \text{ in product}}{\text{wt \% of } C_{23+} \text{ in feed}} \times 100 \quad (3)$$

$$(C_{10} - C_{22})\ \text{selestivity (\%)} = \frac{\text{wt \\% of } C_{10} - C_{22} \text{ in product} - \text{wt \\% of } C_{10} - C_{22} \text{ in feed}}{\text{wt \\% of } C_{23+} \text{ in feed} - \text{wt \\% of } C_{23+} \text{ in product}} \times 100 \quad (4)$$

3. RESULTS AND DISCUSSION

3.1. Structure and Morphology. Figure 1 shows the powder XRD patterns of the as-synthesized samples. AS-20, AS-40, and AS-47 samples obtained after 20, 40, and 47 h of hydrothermal treatment respectively, showed only one broad hump at 2θ = 15−30°, characteristic of amorphous silica (PDF#79-1910).[27] No crystalline alumina phases were detected, indicating that the aluminum element was uniformly incorporated throughout the amorphous silicon oxide.[28,29] Upon hydrothermal treating, this broad hump slightly shifts to a higher angle (Figure 1 inset), indicating the formation of a smaller aluminosilicate ring structures.[29] As the induction period increases to 55 and 62 h, weak diffraction peaks start to gradually appear at 2θ = 7.9, 8.8 and 23.1°, indicating the presence of partial crystallization. Particularly, characteristic diffraction peaks of the MFI structure were observed at 2θ = 7.9, 8.8, 23.1, 24.0, and 24.4° after extending the hydrothermal treatment time to 96 h, indicating the crystal formation of ZSM-5 zeolite.[7]

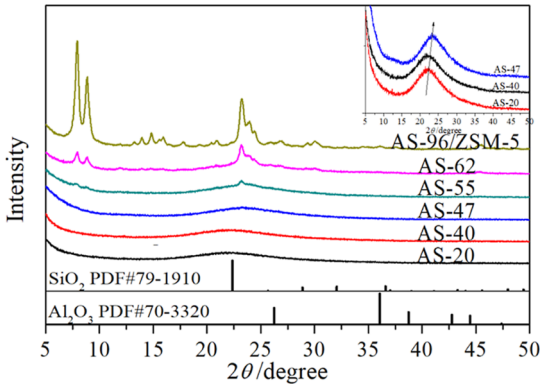

Figure 1. Powder XRD patterns of the as-prepared carrier samples.

The morphology of these ASAs samples was evaluated by using SEM and TEM (Figure 2). The SEM examination (Figure 2a) shows that the amorphous samples consist of nanoparticles with irregular shapes. As shown in Figure 2a-2,

https://doi.org/10.1021/acsomega.4c05594
ACS Omega 2024, 9, 36741−36750

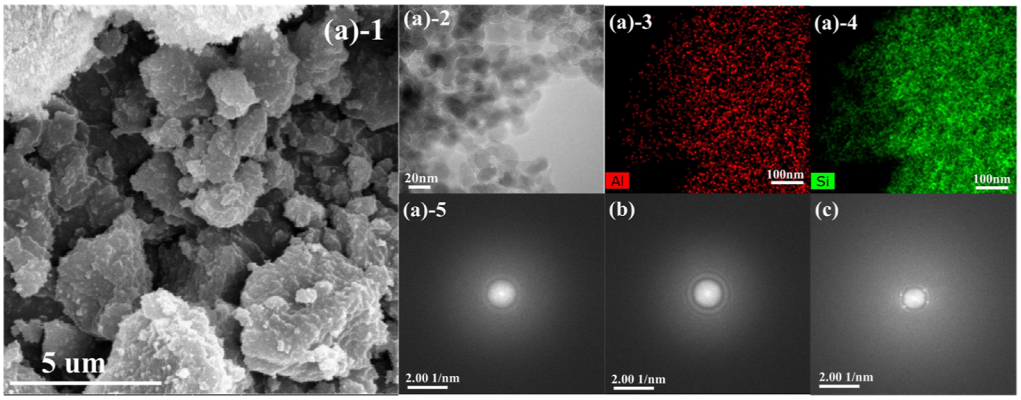

Figure 2. (a-1) SEM image of AS-20, TEM images of (a-2−5) AS-20, (b) AS-47, and (c) AS-62.

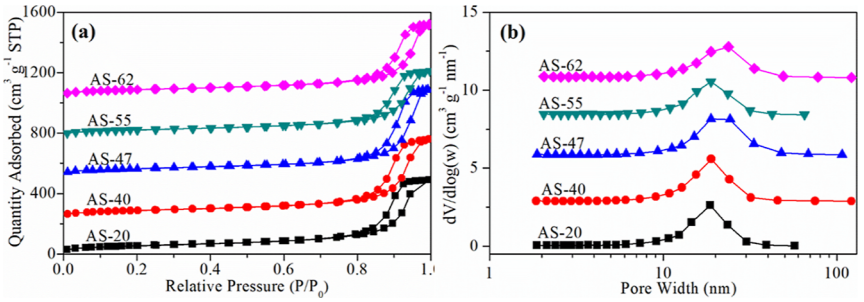

Figure 3. (a) N_2 adsorption−desorption curve and (b) BJH adsorption mesopore size distribution of different ASAs supports.

no aluminum or alumina phase was detected on the sample surface, confirming its amorphous nature. Energy dispersive X-ray (EDX) atom mapping images characterized by STEM (Figure. 2a-3,4) further confirm the homogeneity of the samples on the nanoscale, in agreement with XRD analysis.[30] Although there is no visible lattice in the samples of AS-20, AS-47 (Figure 2a-5,b), the different planar distances observed in EDX spectroscopic imaging demonstrates the existence of molecularly ordered framework atoms.[30] Upon heating, typical selected-area electron diffraction patterns of AS-62 contain discrete diffraction spots (Figure 2c), strongly suggesting the presence of zeolite periodic structure.[31]

The N_2 adsorption−desorption isotherms and pore size distribution for all samples are depicted in Figure 3. Obviously, the N_2 uptake in the low-pressure region ($P/P_0 < 0.01$) is quite low, demonstrating few micropores in the as-synthesized ASAs samples.[32] The subsequent rise in N_2 uptake at higher pressures could put down to the multilayer adsorption, indicating the presence of many mesopores.[32] From the pore distributions shown in Figure 3b, well-distributed mesopores (about 20 nm) are presented in the ASAs samples, likely formed by the ordered framework atoms, secondary structure units and nanoparticles.[20] The detailed textural properties are shown in Table 1. As indicated in the column 3 of table, the BET surface area of the as-prepared ASAs samples is mainly from the external surface, since the mixed oxide nanoparticles observed in SEM organized themselves into mesoporous structures.[33] With increasing hydrothermal synthesis time, the microporous area and pore volume gradually increase, while the external surface area and mesoporous pore volume tend to decrease. The average pore size of ASAs samples was larger than 14 nm, further illustrating their high external surface area and significant porosity characteristics.[9]

Table 1. Textural Properties of a Series of ASAs Samples

samples	BET surface area (m^2/g)			pore volume (cm^3/g)		D_{pore} (nm)
	micropore	external	total	V_{Meso}	V_{Mic}	
AS-20	37	159	196	0.762	0.0157	14.2
AS-40	38	154	192	0.785	0.0159	15.6
AS-47	44	144	188	0.740	0.0189	15.2
AS-55	61	139	200	0.683	0.0280	14.5
AS-62	87	142	230	0.664	0.0409	14.6

3.2. Acidic Properties. The NH_3-TPD profiles of ASAs samples are depicted in Figure S1 of the Supporting Information. The peaks observed can be divided into two groups of acid sites with varying acidic strengths. Generally, the temperature range of weak acid sites is set at 200−250 °C, and that of strong acid sites is 350−400 °C.[32] Apparently, the NH_3-TPD desorption peak gradually increased from AS-20 to AS-62, indicating an increase in the acidic sites with prolonged hydrothermal treatment. Previous studies have reported the preparation of ASAs using beta and Y precursors, but their focus was on physicochemical properties rather than the structure−activity relationship.[34,35] The unique acidic and textural properties of ASAs are attributed to the SiO_4 and AlO_4 tetrahedra structural units and the zeolite-like connectivity in assembling into the mesoporous structures.[34,35]

The type, strength, and density of acid sites were further analyzed by conventional Py-FTIR, with relevant results shown in Table 2. The total medium strong and strong Brønsted acid sites density obtained at desorption temperatures of 200 and 350 °C respectively, follow a decreasing trend in AS-62 > AS-55 > AS-47 > AS-40 > AS-20. It is well-known that the Brønsted acid properties including their location and accessibility, are crucial for catalytic performance, especially

https://doi.org/10.1021/acsomega.4c05594
ACS Omega 2024, 9, 36741−36750

Table 2. Acidity Properties of the Different Samples Obtained by Py-FTIR and DMPy-Py-FTIR

samples	total Brønsted[a]		total Lewis[a]		micropore Brønsted[b]		external Brønsted[c]	
	200 °C	350 °C	200 °C	350 °C	200 °C	350 °C	200 °C	350 °C
AS-20	16.7	1.6	23.3	22.4	1.3	0.7	15.3	0.8
AS-40	18.9	6.0	24.9	17.9	8.7	5.9	10.3	0.1
AS-47	22.9	7.3	23.4	17.6	17.2	5.0	5.7	2.3
AS-55	32.1	10.5	28.2	21.3	16.1	6.2	15.9	4.3
AS-62	44.9	25.3	46.4	26.3	20.1	16.0	24.8	9.2

[a]Determined by Py-FTIR characterization. [b]Determined by in situ 2,6-dimethlypyridine/pyridine sorption for FTIR (DMPy-Py-FTIR). [c]Calculated from total Brønsted minus micropore Brønsted.

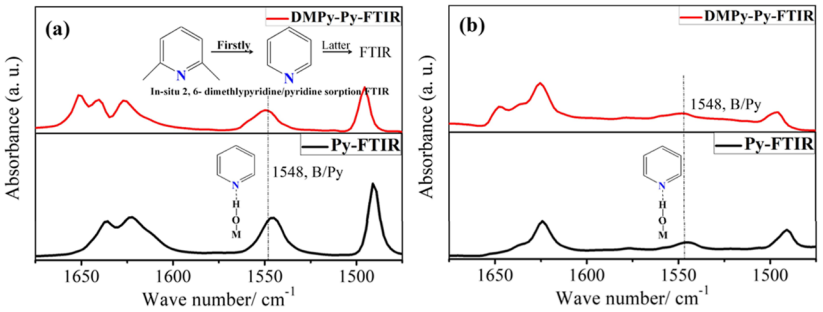

Figure 4. FTIR spectra of AS-47 adsorbed Py and DMPy, Py after desorption at (a) 200 and (b) 350 °C.

in acid-catalyzed bulky molecular processes.[36] Hence, a facile DMPy-Py-FTIR method was utilized to quantify the acid sites inside and outside the micropore. As plotted in Figure 4, the band at 1548 cm^{-1} can be attributed to the C−N stretching of Py ions at Brønsted acid sites.[18,37] Notably, probe molecule DMPy with a kinetic diameter of 0.67 nm is too large to enter the pore channel of 10-MR ZSM-5 (0.51 × 0.55 nm and 0.53 × 0.56 nm).[18,37] The macromolecules DMPy adsorbed in situ occupy all and only the Brønsted acid sites located on external surfaces. Consequently, the amount of Py detected after desorption treatments at 200 and 350 °C in the subsequent Py-FTIR test is defined as medium-strong Brønsted acid and strong Brønsted acid within the micropores, respectively. As listed in columns 6 and 7 of Table 2, the density of the strong Brønsted acid sites inside microporous (Micropore Brønsted, 350 °C) obeys following sequence: AS-62 > AS-55 ≈ AS-40 > AS-47 > AS-20. Both Py-FTIR and DMPy-Py-FTIR tests provide quantified Brønsted acid site density information with a unit of μmol Py/g, thus allowing the calculation of acid site density on the external surface. The corresponding results are presented in the column 8 of Table 2 (External Brønsted, 200 °C), showing a decreasing trend: AS-62 > AS-55 ≈ AS-20 > AS-40 > AS-47.

3.3. Coordination Properties. First, ^{1}H DQ NMR was used to directly obtain hydroxyl group information on ASAs samples to discover the reasons for differences in their physicochemical properties, as shown in Figure 5. A weak autocorrelation peak at (4.3, 8.6) ppm is visible in the AS-20 sample, indicating the presence of zeolitic bridging Si−OH−Al structures as well as Brønsted acid sites.[38] An additional autocorrelation peak at (2.6, 5.2) ppm verifies the strong spatial proximity between oxoaluminum cations [such as AlO^{+}, $Al(OH)^{2+}$, and $AlOH^{2+}$] and terminal SiOH groups, a source of Brønsted acid sites.[38] Upon hydrothermal treating, a strong signal at (4.3, 8.6) in both AS-47 and AS-62 samples provides evidence for the Brønsted acid sites in the super cage, suggesting the presence of zeolitic secondary building units as well as a ZSM-5-like periodic structure.[38] A peak at (2.0, 4.0) ppm is visible, indicative of the spatial proximity of terminal SiOH groups.[39,40] Moreover, the autocorrelation peak at (2.9, 5.8) can be attributed to different types of AlOH groups associated with neutral species, such as AlOOH and $Al(OH)_3$, or extraframework aluminum (EFAL) species, such as AlO^{+}, $Al(OH)^{2+}$ and $AlOH^{2+}$, normally contributing to the Lewis acid sites.[40]

^{27}Al combined with ^{29}Si MAS NMR measurements were carried out to gain insights into the atomic-scale coordination environment of these samples. Typically, the resonance signals of octahedrally coordinated aluminum (Al^{VI}) are present within −10 to 20 ppm, the tetrahedrally coordinated aluminum (Al^{IV}) are in the range of 40−60 ppm, and the penta-coordinated aluminum (Al^{V}) are from 20 to 45 ppm. As shown in Figure 6, most aluminum species are in the form of Al^{IV}, suggesting that the aluminum source reacted with silicates, and then become aluminosilicates with Al^{VI}.[29] It is widely accepted that the chemical shift in NMR signals is highly sensitive to Al−O−Si bond angles.[29] Upon heating between 47 and 96 h, the observed low-field shift of NMR peak (see Figure 7, left axis) indicates a decrease in the average Al−O−Si angles.[29] Figure 7 (right axis) illustrates the variation in full width at half-maximum (fwhm) of the Al^{IV} peak. The fwhm clearly decreased when the hydrothermal treatment time was extended from 20 to 55 h, indicating that aluminosilicates became more structurally ordered, reflected by narrower distributions of Al−O−Si angles.[41] With prolonged hydrothermal treatment over 55 h, the fwhm further decreased rapidly, suggesting the formation of well-ordered aluminosilicates (Figure 7, right axis).

Figure 8 shows ^{29}Si MAS NMR spectra of all of the as-prepared ASAs samples. The main peak signal appears at around $\delta = -100$ ppm corresponds to $Q^4(1Al)$ or $Q^4(2Al)$ silicon species, hinting at a substitution of the silicon sites by aluminum species, even in the vicinity of silanol groups.[29] This aluminum incorporation resulted in a homogeneous mixing of Si and Al atoms at the nanoscale, which aligns well with the findings from XRD, TEM spectroscopy, and ^{1}H DQ NMR

https://doi.org/10.1021/acsomega.4c05594
ACS Omega 2024, 9, 36741−36750

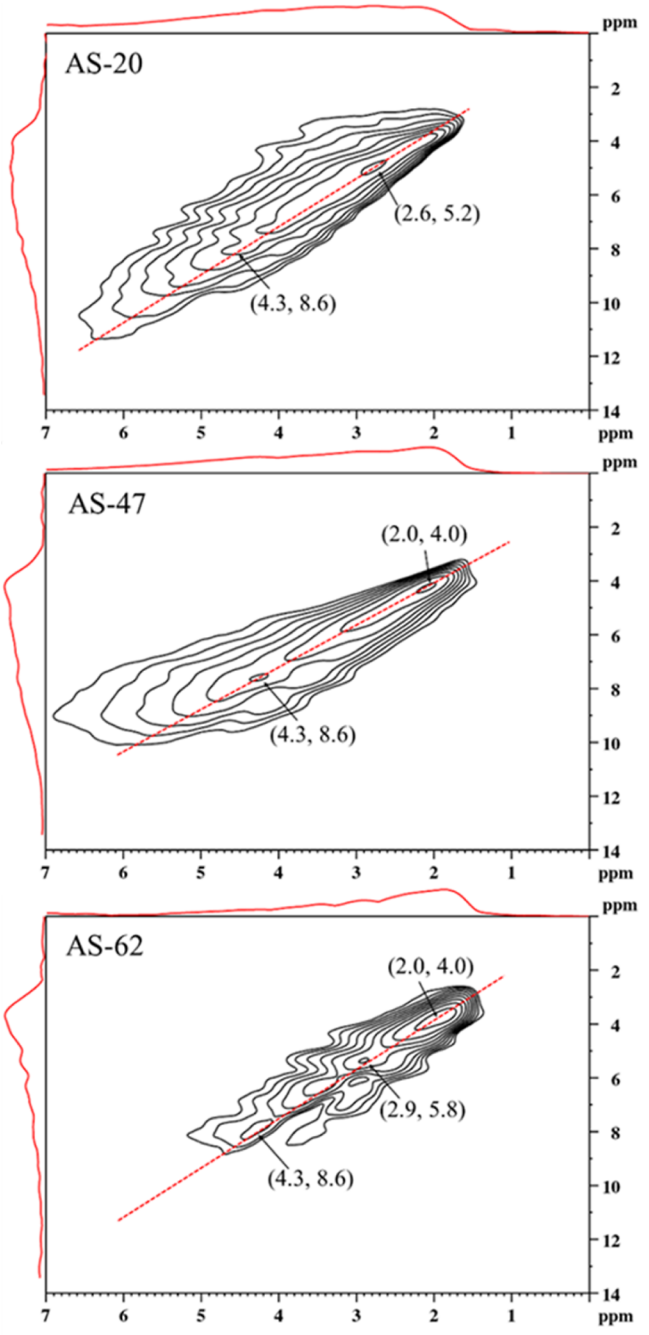

Figure 5. ^{1}H DQ NMR spectra of the several as-synthesized ASAs samples.

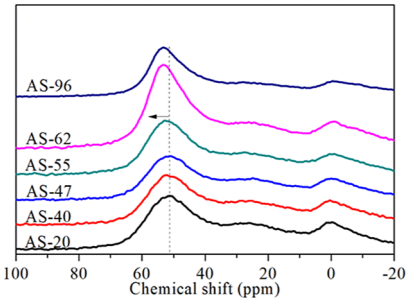

Figure 6. ^{27}Al MAS NMR spectrum of ASAs samples.

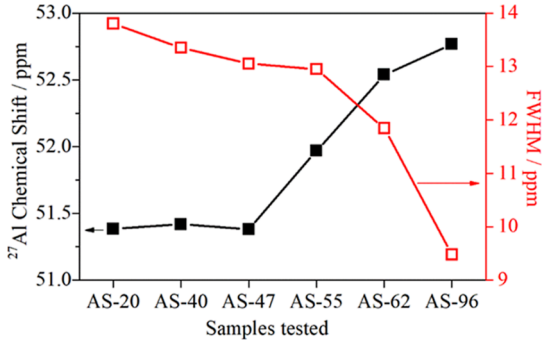

Figure 7. NMR peak position changes of Al^{IV} (left axis; filled black symbols) and maximum half-width changes (right axis; empty red symbols) in the as-synthesized ASAs samples.

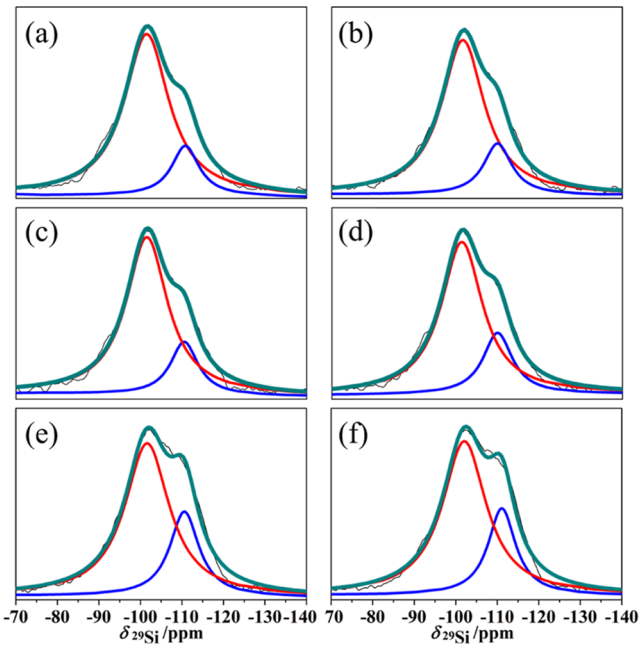

Figure 8. ^{29}Si MAS NMR spectrum of different ASAs supports (a) AS-20, (b) AS-40, (c) AS-47 (d) AS-55, (e) AS-62, and (f) AS-96.

analysis. Additionally, the signal intensity at approximately −110 ppm shows a tendency to increase with prolonged hydrothermal treatment, suggesting an increase in Q^4(0Al) species, evidence for the enhanced structural well-ordered aluminosilicates as well as the formation of ZSM-5 zeolite crystals.[11]

3.4. Catalytic Performance. For hydro-conversion catalyzed by a bifunctional metal/acid catalyst, the rate-determining step is the formation of β-scission of carbenium ions and the skeletal rearrangement at Brønsted acid sites, when the metal function is sufficient.[42,43] It is widely accepted that a 0.5 wt % Pt loading could provide adequate (de)hydrogenation activity to match the acidic isomerization-cracking function.[10,44]

The FTS wax conversions for the as-synthesized catalysts are plotted as a function of the reaction temperature in Figure 9. The conversion rates of all catalysts increase gradually with rising reaction temperatures, a typical behavior in *n*-alkane hydrocracking.[28] The temperature required to achieve 50% conversion for the Pt/AS-*x* catalysts decreases in the following trend of Pt/AS-47 > Pt/AS-40 > Pt/AS-20 ≈ Pt/AS-55 > Pt/

https://doi.org/10.1021/acsomega.4c05594
ACS Omega 2024, 9, 36741−36750

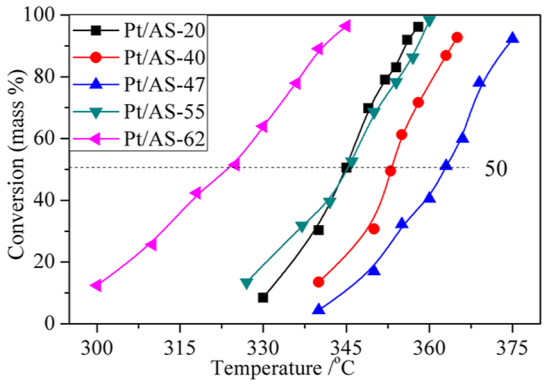

Figure 9. Hydrocracking of FTS wax over Pt/AS-*x* catalysts at different temperatures.

AS-62. It is well-recognized that for a bifunctional catalyst with sufficient metal functionality, the acidic nature of the carriers, particularly the Brønsted acidity, is critical for catalytic performance.[8,45] To systematically investigate the acidity-activity performance relationship, Figure 10 plots the temperature required to achieve 50% conversion versus total and external medium-strong Brønsted acid density. As shown, the activities of all catalyst samples correspond to the density of external medium strong Brønsted acid sites (Ex-Brønsted, 200 °C). And the higher the number of these acidic sites, the lower the reaction temperature required for the corresponding catalyst, validating the utility of the Py-FTIR and DMPy-Py-FTIR techniques. It is a consensus that the effective active sites have to be accessible.[46] Although FTS wax could penetrate the micropores, significant free-energy diffusion barriers must be overcome to reach the accessible active sites due to inevitable skeletal isomerization and steric hindrance from the microporous system.[2,47] Accordingly, in our reaction system, these bulky FTS wax compounds tend to react on the external surfaces, facing a smaller free energy barrier than diffusing into the micropores.[2,48] The more Brønsted acid sites located on external surfaces, the faster the olefin intermediates are protonated, the easier the cracking reaction can occur, and the higher the corresponding catalytic activity.

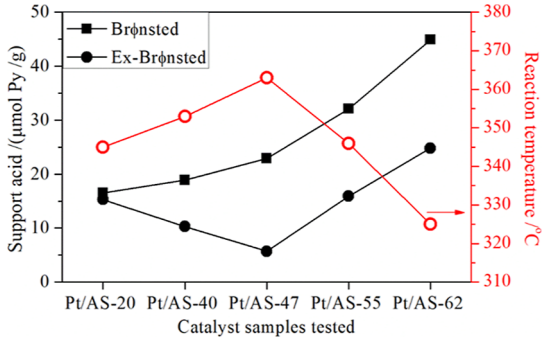

Figure 10. Relationship between the reaction temperature required to achieve about 50% conversion and the Brønsted acid state in ASAs supports.

Figure S2 of the Supporting Information exhibits the selectivity of diesel as a function of the corresponding conversion obtained at different reaction temperatures. Throughout the test interval, the diesel selectivity decreases with increasing conversion, which is common in the hydrotreating of *n*-alkanes.[44] A more detailed analysis of FTS wax hydrocracking for the five representative catalysts is given in Table 3. As shown, the selectivity to diesel decreases in the trend of Pt/AS-20 > Pt/AS-40 ≈ Pt/AS-55 > Pt/AS-47 > Pt/AS-62. It has been proven that the selectivity behavior generally correlates with the strength of the carrier acidic sites as well as the diffusion of reaction intermediates for the bifunctional catalysts with sufficient metal functionality. At this point, the relationship between the density of strong Brønsted acid sites inside and outside the micropores and the products selectivity is plotted in Figure 11. As shown, the strong Brønsted acid sites in micropores were negative to diesel selectivity, and the higher the density, the lower the selectivity for diesel. FTS wax compounds are prone to cracking and

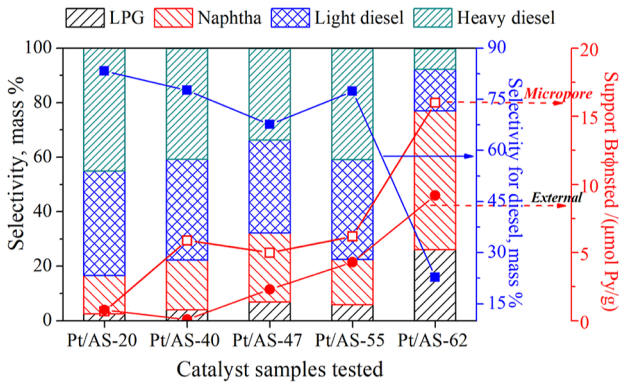

Figure 11. Relationship between the selectivity for diesel and the properties of Brønsted acid in the supports at a conversion rate of about 50%.

Table 3. Comparison of Hydrocracking of FT Wax at about 50% Conversion over Different Catalysts[a]

		Pt/AS-20	Pt/AS-40	Pt/AS-47	Pt/AS-55	Pt/AS-62
temperature (°C)		345	353	363	346	325
conversion (%)		50.5	49.3	51.1	52.6	51.5
selectivity (wt %)	dry gas	0.06	0.14	0.15	0.14	0.25
	LPG	2.5	4.0	6.9	5.8	26.1
	naphtha (<150°C)	14.2	18.3	25.4	16.7	50.9
	diesel (150−280 °C)	38.3	37.0	34.0	36.6	15.3
	diesel (280−370 °C)	45.0	40.6	33.6	40.8	7.5
	diesel	83.3	77.6	67.6	77.4	22.8
diesel yield (%)		42.1	38.4	34.6	40.7	11.7
liquid yield (%)		97.4	93.5	92.7	88.9	76.3

[a]Condensates at 4.0 MPa, LHSV = 1.0 h^{-1}, and H_2/oil = 1000 (volume ratio).

https://doi.org/10.1021/acsomega.4c05594
ACS Omega 2024, 9, 36741−36750

often undergo secondary cracking to produce diesel fractions.[17] Moreover, compared to the longer carbon-chain FTS wax, the primary cracking products ($<C_{40}$) from first hydrocracking could diffuse into the micropores easier.[48,49] Due to the steric hindrance from microporous system and the stronger adsorption at strong acid sites, these primary cracking products may be trapped inside once diffused in micropores, causing prolonged retention times as well as excessive formation of light fractions such as naphtha and LPG.[17,50] Hence, the strong Brønsted acid sites in micropores were not conducive to diesel production. Among the tested catalysts, the Pt/AS-20 with few intramicropore Brønsted acid sites shows the highest diesel selectivity (83.3%), higher than that of Pt/SA-10 (78.7%) obtained from a precursor of Beta zeolite in our previous work, surpassing the general view that larger pores favor the heavy cracking fractions production.[17] Given the larger pore size of the 12-MR channels, the 10-MR from ZSM-5 zeolite effectively inhibits the diffusion of primary cracking products into micropores due to steric hindrance, reducing the likelihood and extent of multicracking. These ASAs samples obtained from the mother liquid of 10-MR MFI zeolite are generally more selective for heavy diesel and less selective for naphtha. This not only demonstrates their superiority but also validates the importance of the relatively small 10-MR channels in maximizing diesel selectivity by preventing the multicracking of primary cracking products.

4. CONCLUSIONS

High-performance ASAs were synthesized prior to the formation of the 10-MR ZSM-5 zeolite by regulating the hydrothermal processing time. The special acidic and textural properties are attributed to the SiO_4 and AlO_4 tetrahedra structural units and the zeolite-like connectivity maintained during their assembly into mesoporous structures. A facile FTIR method of in situ adsorbing DMPy followed by Py adsorption was utilized to quantify the Brønsted acid sites in the micropores. This method effectively minimized the influence of IMEC, and enhanced the accuracy of the acid characterization results. The structure−activity relationship, particularly regarding the strength, density, and location of Brønsted acid sites, was investigated by using hydrocracking of FTS wax to diesel as a model reaction. The evaluation results showed that the external medium strong Brønsted acid sites rather than the total ones played an important role in FTS wax hydrocracking activity. Contrary to the general view that larger pores favor the production of heavy cracking fractions, the as-synthesized ASAs with a 10-MR microporous structure were more positive for diesel production than those with a 12-MR structure. The strong Brønsted acid sites in micropores were not conducive to diesel production mainly due to the stronger adsorption and the steric hindrance from the microporous system. Among the catalysts tested, the Pt/AS-20 catalyst with few intramicropore strong Brønsted acid sites exhibited high diesel selectivity (83.3%) at 50.5% conversion under industrially relevant conditions, which provided a good opportunity to develop hydrocracking catalysts more rationally for industrial FTS wax feed.

■ ASSOCIATED CONTENT

Supporting Information

The Supporting Information is available free of charge at https://pubs.acs.org/doi/10.1021/acsomega.4c05594.

Chemicals and reagents; acidic properties of different ASAs supports upon NH_3-TPD; a correlation between conversion and selectivity for diesel in the hydrocracking of FTS wax (PDF)

■ AUTHOR INFORMATION

Corresponding Authors

Zhichao Tao − *National Energy Research Center for Clean Fuels, Synfuels China Co., Ltd., Beijing 101400, China;* Present Address: Synfuels China Technology Co. Ltd. Leyuan South Street II, No.1 Yanqi Economic Development Zone C# Huairou District, Beijing 101407 China; orcid.org/0000-0002-0516-1503; Email: zhichaotao@163.com

Yong Yang − *National Energy Research Center for Clean Fuels, Synfuels China Co., Ltd., Beijing 101400, China;* Present Address: Synfuels China Technology Co. Ltd. Leyuan South Street II, No.1 Yanqi Economic Development Zone C# Huairou District, Beijing 101407 China; orcid.org/0000-0002-9220-6166; Email: yyong@sxicc.ac.cn

Authors

Tao Li − *School of Bioengineering, Shandong Polytechnic, Jinan 250104, China*

Shuyuan Wang − *Energy Research Institute, Qilu University of Technology (Shandong Academy of Sciences), Jinan 250014, China*

Zhenye Sun − *Qingdao Product Quality Testing Research Institute, Qingdao 266100, China*

Yan Wang − *School of Bioengineering, Shandong Polytechnic, Jinan 250104, China*

Jinghong Su − *School of Bioengineering, Shandong Polytechnic, Jinan 250104, China*

Yinghui Lv − *School of Bioengineering, Shandong Polytechnic, Jinan 250104, China*

Ling Zhang − *National Energy Research Center for Clean Fuels, Synfuels China Co., Ltd., Beijing 101400, China*

Complete contact information is available at: https://pubs.acs.org/10.1021/acsomega.4c05594

Author Contributions

T.L. contributed to formal analysis, writing-original draft, and resources. S.W., J.S., and Z.S. contributed to investigation and validation. Y.W., Y.L., and L.Z. contributed to writing-editing, and conceptualization. Z.T. contributed to conceptualization. Y.Y. contributed to writing-review.

Notes

The authors declare no competing financial interest.

■ ACKNOWLEDGMENTS

We thank for the financial support from the National Natural Science Foundation of China (22025804) and Natural Science Foundation of Shandong Province of China (ZR2022QB184), Zhungeer Science and Technology Project (2023CG-01), Jinan City Municipal School Integration Development Strategy Project (JNSX2023097). We also acknowledge R&D Center for New Technology of Biological Drugs and Health Engineering in Shandong Higher Education Institutions.

REFERENCES

(1) Zhang, W.; Zhang, H.; Abbas, M.; Zhang, J.; Huang, Z.; Kawi, S.; Chen, J. Eco-friendly solid-state synthesis of Na-promoted Mn-Fe/ZrO2 catalyst for Fischer−Tropsch synthesis. *Fuel* **2024**, *363*, 131013.

(2) Bouchy, C.; Hastoy, G.; Guillon, E.; Martens, J. A. Fischer−Tropsch Waxes Upgrading via Hydrocracking and Selective Hydroisomerization. *Oil Gas Sci. Technol.* **2009**, *64* (1), 91−112.

(3) Tomasek, S.; Lónyi, F.; Valyon, J.; Hancsók, J. Fuel purpose hydrocracking of biomass based Fischer−Tropsch paraffin mixtures on bifunctional catalysts. *Energy Convers. Manage.* **2020**, *213*, 112775.

(4) Zhao, J.; Wang, X.; Niu, H.; Liu, J.; Liang, C.; Li, C. Hydroisomerization Principles of Acenaphthene to Alkyladamantanes over Modified USY-Supported Pt Catalysts. *Energy Fuels* **2024**, *38*, 7181−7195.

(5) Wang, Q.; Shan, H.; Sim, L. B.; Xie, J.; Ye, S.; Fu, J.; Wang, J.; Zhang, N.; Zheng, J.; Chen, B. ZSM-22 Synthesized Using Structure-Directing Agents of Different Alkyl Chain Lengths for Controlled n-Hexadecane Hydroisomerizations. *Ind. Eng. Chem. Res.* **2023**, *62* (29), 11470−11479.

(6) Hengsawad, T.; Srimingkwanchai, C.; Butnark, S.; Resasco, D. E.; Jongpatiwut, S. Effect of Metal-Acid Balance on Hydroprocessed Renewable Jet Fuel Synthesis from Hydrocracking and Hydroisomerization of Biohydrogenated Diesel over Pt-Supported Catalysts. *Ind. Eng. Chem. Res.* **2018**, *57* (5), 1429−1440.

(7) Zhou, A.; Zhang, J.; Shang, S.; Yang, H.; Zhang, A.; Song, C.; Guo, X. Tuning Pt Location and Intimacy between Pt-Acid Active Sites in Pt/ZSM-5 Bifunctional Catalysts for Effective Alkylation of Benzene with Ethane. *Ind. Eng. Chem. Res.* **2024**, *63* (2), 990−999.

(8) Seo, M.-g.; Lee, D.-W.; Lee, K.-Y.; Moon, D. J. Pt/Al-SBA-15 catalysts for hydrocracking of C_{21}-C_{34} n-paraffin mixture into gasoline and diesel fractions. *Fuel* **2015**, *143*, 63−71.

(9) Feng, W.; Zheng, B.; Cui, Q.; Wang, T.; Yuan, P.; Zhu, H.; Yue, Y.; Bao, X. Influence of ASA composition on its supported Mo catalyst performance for the slurry-phase hydrocracking of vacuum residue. *Fuel* **2022**, *324*, 124628.

(10) Meng, L.; Vanbutsele, G.; Pestman, R.; Godin, A.; Romero, D. E.; van Hoof, A. J. F.; Gao, L.; Kimpel, T. F.; Chai, J.; Martens, J. A.; Hensen, E. J. M. Mechanistic aspects of n-paraffins hydrocracking: Influence of zeolite morphology and acidity of Pd(Pt)/ZSM-5 catalysts. *J. Catal.* **2020**, *389*, 544−555.

(11) Pölczmann, G.; Valyon, J.; Szegedi, A. ·; Mihályi, R. M.; Hancsók, J. Hydroisomerization of Fischer−Tropsch Wax on Pt/AlSBA-15 and Pt/SAPO-11 Catalysts. *Top. Catal.* **2011**, *54* (16−18), 1079−1083.

(12) Liu, Y.; Murata, K.; Okabe, K.; Inaba, M.; Takahara, I.; Hanaoka, T.; Sakanishi, K. Selective Hydrocracking of Fischer−Tropsch Waxes to High-quality Diesel Fuel Over Pt-promoted Polyoxocation-pillared Montmorillonites. *Top. Catal.* **2009**, *52* (6−7), 597−608.

(13) Lee, J.; Hwang, S.; Seo, J. G.; Hong, U. G.; Jung, J. C.; Song, I. K. Pd catalyst supported on SiO_2-Al_2O_3 xerogel for hydrocracking of paraffin wax to middle distillate. *J. Ind. Eng. Chem.* **2011**, *17* (2), 310−315.

(14) Bao, J.; Yang, Q.-h.; Zeng, S.-q.; Sang, X.-y.; Zhai, W.-m.; Nie, H. Synthesis of amorphous silica-alumina with enhanced specific surface area and acidity by pH-swing method and its catalytic activity in cumene cracking. *Microporous Mesoporous Mater.* **2022**, *337*, 111897.

(15) Cui, W.; Li, W.; Gao, R.; Ma, H.; Li, D.; Niu, M.; Lei, X. Hydroprocessing of Low-Temperature Coal Tar for the Production of Clean Fuel over Fluorinated NiW/Al_2O_3-SiO_2 Catalyst. *Energy Fuels* **2017**, *31* (4), 3768−3783.

(16) Ayandiran, A. A.; Boahene, P. E.; Nanda, S.; Dalai, A. K.; Hu, Y. Hydroprocessing of oleic acid for the production of aviation turbine fuel range hydrocarbons over bimetallic Fe-Cu/SiO2-Al2O3 catalysts promoted by Sn, Ti and Zr. *Mol. Catal.* **2022**, *523*, 111358.

(17) Li, T.; Tao, Z.; Hu, C.; Zhao, C.; Yi, F.; Zhao, G.; Zhang, L.; Yang, Y. Brønsted acidity of amorphous silica-aluminas for hydrocracking of Fischer−Tropsch wax into diesel fractions. *Appl. Catal., A* **2022**, *630*, 118439.

(18) Holm, M. S.; Svelle, S.; Joensen, F.; Beato, P.; Christensen, C. H.; Bordiga, S.; Bjørgen, M. Assessing the acid properties of desilicated ZSM-5 by FTIR using CO and 2,4,6-trimethylpyridine (collidine) as molecular probes. *Appl. Catal., A* **2009**, *356* (1), 23−30.

(19) Thibault-Starzyk, F.; Stan, I.; Abelló, S.; Bonilla, A.; Thomas, K.; Fernandez, C.; Gilson, J.-P.; Pérez-Ramírez, J. Quantification of enhanced acid site accessibility in hierarchical zeolites-The accessibility index. *J. Catal.* **2009**, *264* (1), 11−14.

(20) Liu, S.; Ren, J.; Zhang, H.; Lv, E.; Yang, Y.; Li, Y.-W. Synthesis, characterization and isomerization performance of micro/mesoporous materials based on H-ZSM-22 zeolite. *J. Catal.* **2016**, *335*, 11−23.

(21) Li, Y.; Sun, J.; Wei, J.; Mu, C.; Zhao, Y.; Wang, S.; Ma, X. Cascade hydrogenation of n-C16 to produce jet fuel over tandem catalysts of modified ZSM-22. *J. Ind. Eng. Chem.* **2022**, *111*, 88−97.

(22) Chen, Z.; Liu, S.; Wang, H.; Ning, Q.; Zhang, H.; Yun, Y.; Ren, J.; Li, Y.-W. Synthesis and characterization of bundle-shaped ZSM-22 zeolite via the oriented fusion of nanorods and its enhanced isomerization performance. *J. Catal.* **2018**, *361*, 177−185.

(23) Datka, J.; Turek, A. M.; Jehng, J. M.; Wachs, I. E. Acidic properties of supported niobium oxide catalysts: An infrared spectroscopy investigation. *J. Catal.* **1992**, *135*, 186−199.

(24) Emeis, C. A. Determination of Integrated Molar Extinction Coefficients for Infrared Absorption Bands of Pyridine Adsorbed on Solid Acid Catalysts. *J. Catal.* **1993**, *141*, 347−354.

(25) Wu, G.; Hu, Y.; Bao, Q.; Zhang, J.; Ge, J. Improved Catalytic Performances of the NaOH-Treated ZSM-22 Zeolite in the 1-Butene Skeletal Isomerization Reaction: Effect of External Acid Sites. *ACS Omega* **2023**, *8* (16), 14349−14364.

(26) Hasanudin, H.; Asri, W. R.; Mara, A.; Al Muttaqii, M.; Maryana, R.; Rinaldi, N.; Sagadevan, S.; Zhang, Q.; Fanani, Z.; Hadiah, F. Enhancement of Catalytic Activity on Crude Palm Oil Hydrocracking over SiO_2/Zr Assisted with Potassium Hydrogen Phthalate. *ACS Omega* **2023**, *8* (23), 20858−20868.

(27) Wang, Y.-J.; Liu, C.; Wu, Y.-J.; Song, Y.-H.; Zhu, M.-L.; Huang, J.; Liu, Z.-T.; Liu, Z.-W. Flame-spray-pyrolysis amorphous alumina-silica for tailoring the product distribution of Fischer−Tropsch synthesis. *Catal. Today* **2020**, *339*, 40−47.

(28) Li, T.; Zhang, L.; Tao, Z.; Hu, C.; Zhao, C.; Yi, F.; Gao, X.; Wen, X.; Yang, Y.; Li, Y. Synthesis and characterization of amorphous silica-alumina with enhanced acidity and its application in hydroisomerization/cracking. *Fuel* **2020**, *279*, 118487.

(29) Ikuno, T.; Chaikittisilp, W.; Liu, Z.; Iida, T.; Yanaba, Y.; Yoshikawa, T.; Kohara, S.; Wakihara, T.; Okubo, T. Structure-Directing Behaviors of Tetraethylammonium Cations toward Zeolite Beta Revealed by the Evolution of Aluminosilicate Species Formed during the Crystallization Process. *J. Am. Chem. Soc.* **2015**, *137* (45), 14533−14544.

(30) Brouwer, D. H.; Cadars, S.; Eckert, J.; Liu, Z.; Terasaki, O.; Chmelka, B. F. A general protocol for determining the structures of molecularly ordered but noncrystalline silicate frameworks. *J. Am. Chem. Soc.* **2013**, *135* (15), 5641−5655.

(31) Zhu, J.; Zhu, Y.; Zhu, L.; Rigutto, M.; van der Made, A.; Yang, C.; Pan, S.; Wang, L.; Zhu, L.; Jin, Y.; Sun, Q.; Wu, Q.; Meng, X.; Zhang, D.; Han, Y.; Li, J.; Chu, Y.; Zheng, A.; Qiu, S.; Zheng, X.; Xiao, F. S. Highly mesoporous single-crystalline zeolite beta synthesized using a nonsurfactant cationic polymer as a dual-function template. *J. Am. Chem. Soc.* **2014**, *136* (6), 2503−2510.

(32) Liu, S.; Ren, J.; Zhu, S.; Zhang, H.; Lv, E.; Xu, J.; Li, Y.-W. Synthesis and characterization of the Fe-substituted ZSM-22 zeolite catalyst with high n-dodecane isomerization performance. *J. Catal.* **2015**, *330*, 485−496.

(33) Hakim, S. H.; Shanks, B. H. Synthesis and characterization of hierarchically structured aluminosilicates. *J. Mater. Chem.* **2011**, *21* (20), 7364−7375.

(34) Liu, Y.; Zhang, W.; Pinnavaia, T. J. Steam-Stable MSU-S Aluminosilicate Mesostructures Assembled from Zeolite ZSM-5 and Zeolite Beta Seeds. *Angew. Chem., Int. Ed.* **2001**, *40* (7), 1255−1258.

https://doi.org/10.1021/acsomega.4c05594
ACS Omega 2024, 9, 36741−36750

(35) Liu, Y.; Zhang, W.; Pinnavaia, T. J. Steam-Stable Aluminosilicate Mesostructures Assembled from Zeolite Type Y Seeds. *J. Am. Chem. Soc.* **2000**, *122*, 8791−8792.
(36) Huang, J.; van Vegten, N.; Jiang, Y.; Hunger, M.; Baiker, A. Increasing the Bronsted acidity of flame-derived silica/alumina up to zeolitic strength. *Angew. Chem., Int. Ed.* **2010**, *49*, 7776.
(37) Nesterenko, N. S.; Thibault-Starzyk, F.; Montouilliout, V.; Yushchenko, V. V.; Fernandez, C.; Gilson, J. P.; Fajula, F.; Ivanova, I. I. The use of the consecutive adsorption of pyridine bases and carbon monoxide in the IR spectroscopic study of the accessibility of acid sites in microporous/mesoporous materials. *Kinet. Catal.* **2006**, *47* (1), 40−48.
(38) Groen, J. C.; Zhu, W.; Brouwer, S.; Huynink, S. J.; Kapteijn, F.; Moulijn, J. A.; Pérez-Ramírez, J. Direct Demonstration of Enhanced Diffusion in Mesoporous ZSM-5 Zeolite Obtained via Controlled Desilication. *J. Am. Chem. Soc.* **2007**, *129*, 355−360.
(39) Corma, A. Inorganic Solid Acids and Their Use in Acid-Catalyzed Hydrocarbon Reactions. *Chem. Rev.* **1995**, *95* (3), 559−614.
(40) Li, S.; Zheng, A.; Su, Y.; Zhang, H.; Chen, L.; Yang, J.; Ye, C.; Deng, F. Brønsted/Lewis Acid Synergy in Dealuminated HY Zeolite: A Combined Solid-State NMR and Theoretical Calculation Study. *J. Am. Chem. Soc.* **2007**, *129*, 11161−11171.
(41) Xu, B.; Sievers, C.; Lercher, J. A.; van Veen, J. A. R.; Giltay, P.; Prins, R.; van Bokhoven, J. A. Strong Brønsted Acidity in Amorphous Silica-Aluminas. *J. Phys. Chem. C* **2007**, *111*, 12075−12079.
(42) Kaka khel, T.; Mäki-Arvela, P.; Azkaar, M.; Vajglová, Z.; Aho, A.; Hemming, J.; Peurla, M.; Eränen, K.; Kumar, N.; Murzin, D. Y. Hexadecane hydrocracking for production of jet fuels from renewable diesel over proton and metal modified H-Beta zeolites. *Mol. Catal.* **2019**, *476*, 110515.
(43) Mu, C.; Sun, J.; Xie, C.; Bao, J.; Guo, X.; Zhang, H.; Zhao, Y.; Wang, S.; Ma, X. Shape Selectivity of AEL Channels for Anomalously Facilitating Biojet Fuel Production from Long-Chain n-Alkane Hydrocracking. *ACS Catal.* **2024**, *14* (3), 1394−1404.
(44) Wang, Y.; Tao, Z.; Wu, B.; Xu, J.; Huo, C.; Li, K.; Chen, H.; Yang, Y.; Li, Y. Effect of metal precursors on the performance of Pt/ZSM-22 catalysts for n-hexadecane hydroisomerization. *J. Catal.* **2015**, *322*, 1−13.
(45) Corma, A.; Martinez, A.; Pergher, S.; Peratello, S.; Perego, C.; Bellusi, G. Hydrocracking-hydroisomerization of n-decane on amorphous silica-alumina with uniform pore diameter. *Appl. Catal., A* **1997**, *152*, 107−125.
(46) Suganuma, S.; Arita, K.; Nakano, F.; Tsuji, E.; Katada, N. Adsorption kinetics in removal of basic nitrogen-containing compounds from practical heavy oils by amorphous silica-alumina. *Fuel* **2020**, *266*, 117055.
(47) Smit, B.; Maesen, T. L. Towards a molecular understanding of shape selectivity. *Nature* **2008**, *451* (7179), 671−678.
(48) Tomasek, S.; Lonyi, F.; Valyon, J.; Wollmann, A.; Hancsok, J. Hydrocracking of Fischer−Tropsch Paraffin Mixtures over Strong Acid Bifunctional Catalysts to Engine Fuels. *ACS Omega* **2020**, *5* (41), 26413−26420.
(49) Sie, S. T. Acid-Catalyzed Cracking of Paraffinic Hydrocarbons. 3. Evidence for the Protonated Cyclopropane Mechanism from Hydrocracking/Hydroisomerization Experiments. *Ind. Eng. Chem. Res.* **1993**, *32* (3), 403−408.
(50) Verheyen, E.; Jo, C.; Kurttepeli, M.; Vanbutsele, G.; Gobechiya, E.; Korányi, T. I.; Bals, S.; Van Tendeloo, G.; Ryoo, R.; Kirschhock, C. E. A.; Martens, J. A. Molecular shape-selectivity of MFI zeolite nanosheets in n-decane isomerization and hydrocracking. *J. Catal.* **2013**, *300*, 70−80.

https://doi.org/10.1021/acsomega.4c05594
ACS Omega 2024, 9, 36741−36750